

Photometry and Angles Data For Spacecraft Relative Navigation

Matthew P. Whittaker,^{*} Richard Linares,[†] and John L. Crassidis[‡]

University at Buffalo, State University of New York, Amherst, NY, 14260-4400

This paper proposes a new approach for relative navigation of formation flying spacecraft. This approach utilizes azimuth and elevation angle information as well as light intensity data gathered from a photometric sensor to estimate the relative position and velocity between collaborating spacecraft. A basic measurement model simulates the deputy spacecraft as a simple sphere that only reflects light diffusely. An Unscented Kalman Filter is successfully used for state estimation and subsequently shows the initial proof of concept. This study motivates further investigation into the potential for using this new approach for inexpensive and reliable relative navigation systems.

I. Introduction

Relative motion between formation flying and rendezvousing spacecraft has been an area of research since the Apollo missions. Many approaches for determining the relative distance between these spacecraft have been attempted since this research started. Resolved images have been used to estimate the size and shape of satellites as well as the relative position and velocity of rendezvousing spacecraft.^{1,2} These approaches work either directly with the image pixels or are used to identify features of the space object (SO). Features, such as corners, edges and markers, are located and tracked temporally to estimate higher level motion and the structure of the rigid body.³ Feature-based approaches rely on continuously identifying and tracking higher level traits of the SO by using a Kalman filter to estimate feature location and motion parameters. Pixel-based methods rely on pixel-level information, and use the shading, texture and optical flow of the images to estimate the relative position at each time step using a monocular camera. Since these methods rely on pixel-level computations they typically involve very high-dimensional states. They are also very computationally expensive due to several issues, such as image segmentation, component labeling and searching for collocated centroids, etc. Furthermore, these methods are also very sensitive to pixel-level detail and are easily corrupted by unpredictable light intensities, reflective material and wrinkled surfaces. They require high resolution of the object to resolve meaningful shape estimates, and therefore are only effective for space-based sensing of objects with small relative distances.

One method for measuring line-of-sight (LOS) observations between multiple vehicles is the vision-based navigation (VISNAV) system.⁴ This consists of an optical sensor combined with a specific light source (beacon) in order to achieve a selective vision. The VISNAV system is applied to the spacecraft formation flying problem in Ref. 5. State estimation is performed using an optimal observer design. An Extended Kalman Filter (EKF) is applied to the VISNAV-based relative spacecraft position and attitude estimation in Ref. 6. Simulations show that accurate estimates of relative position and attitude are possible. The VISNAV system relies on parallax to obtain relative state information. If the distances between the individual beacons is much smaller compared with the relative distance between the vehicles then the beacons effectively become a single point source. This causes the system to become unobservable. Thus, the VISNAV system is typically used for proximity type applications.

^{*}Graduate Student, Department of Mechanical & Aerospace Engineering. Email: mpw6@buffalo.edu. Student Member AIAA.

[†]Graduate Student, Department of Mechanical & Aerospace Engineering. Email: linares2@buffalo.edu. Student Member AIAA.

[‡]CUBRC Professor in Space Situational Awareness, Department of Mechanical & Aerospace Engineering. Email: johnc@buffalo.edu. Associate Fellow AIAA.

Light curves (the SO temporal brightness) have been used to estimate several attributes of an object. For example, light curve approaches have been studied to estimate the shape and state of asteroids.^{7,8} Light curves and thermal emissions have been used to recover the three-dimensional shape of an object assuming its orientation with respect to the observer is known.⁹ The benefits of using a light curve approach over the aforementioned others is that it is not limited to larger objects in lower orbits and it can be applied to small and dim objects in higher orbits, such as geosynchronous spacecraft. Here light curve data is considered for estimating the relative position and velocity of collaborating spacecraft.

There are several aspects of using light curve data (temporal photometry) that make it particularly advantageous for object detection, identification and tracking. Light curve data are the time-varying sensor wavelength-dependent apparent magnitude of energy (i.e. photons) scattered (reflected) off of an object along the line-of-sight to an observer. Because the apparent magnitude of the SO is a function of its size, orientation and surface material properties, one or more of these characteristics should be recoverable from the photometric data. This can aid in the detection and tracking of an SO to allow for relative navigation. Also, the relative distance does not need to be small between the vehicles. Finally, light curve observations can be observed using passive sensors, which reduces the complexity of the overall system.

Absolute attitude estimation using light curve data has been demonstrated in Ref. 10; however, light curve information has not been explored yet for relative navigation. The apparent magnitude obtained from light curves is a function of the distance between the reflecting object and the observer, which in essence provides range information. Active ranging can be accomplished by emitting a signal and obtaining a return. Passive ranging can be accomplished by using the ratio between the sensed area by the imager and the projected area of the target spacecraft, but this requires that the attitude of target to be known. The main goal of this current work is to provide a preliminary study to serve as a proof of concept for using light curve data to determine relative position and velocity of collaborating spacecraft. Note that the only collaboration requirement is that the spectral properties of the target vehicle be known, which is used in the light curve model. But these properties can also be estimated as part of the overall process,¹¹ which can lead to a fully non-collaborating relative navigation approach between two vehicles. Here, angle and light magnitude measurements are used to estimate the relative position of formation flying spacecraft using an Unscented Kalman Filter (UKF). Simulation results are shown to assess the performance of using light curve data in addition to traditional angles data. The main objective is to show that the self-contained and non-emitting realtime approach developed here can be used to 1) provide observability for cases that are traditionally non-observable using angles-only data, and 2) improve the estimation performance by incorporating passively obtained light curve data. Furthermore, it is demonstrated here that the addition of light curve data dramatically improves the performance of estimating the absolute positions of both spacecraft from only relative observations.

The organization of this paper is as follows. First the dynamic models used for relative navigation are summarized. This is followed by showing the models for the assumed measurements, which includes azimuth, elevation and apparent brightness magnitude. Then the basic equations for the UKF are summarized. Finally, simulation results are presented.

II. Relative Navigation Approach

A. Dynamical Model

When dealing with formation flying spacecraft it is most convenient to use the local Hill frame coordinates. This is the frame that is used to describe the relative motion between the two space vehicles. Figure 1 illustrates this local Hill frame; it is defined by the triad $\{\hat{\mathbf{o}}_r, \hat{\mathbf{o}}_\theta, \hat{\mathbf{o}}_h\}$, where the $\hat{\mathbf{o}}_r$ axis points in the radial direction of reference orbit, the $\hat{\mathbf{o}}_h$ axis points in the direction of the angular momentum vector of the reference orbit, and the $\hat{\mathbf{o}}_\theta$ axis is such that it forms a proper orthogonal frame.

The lead spacecraft is typically referred to as the chief spacecraft and the secondary spacecraft is referred to as the deputy spacecraft. The relative position vector pointing from the chief spacecraft towards the deputy is expressed using the components $\boldsymbol{\rho} = [x \ y \ z]^T$, as shown in Figure 1. Using the aforementioned Hill reference frame, and assuming that the relative orbit position coordinates are small compared with respect to the chief orbit radius, the relative position of the deputy spacecraft can be described from the

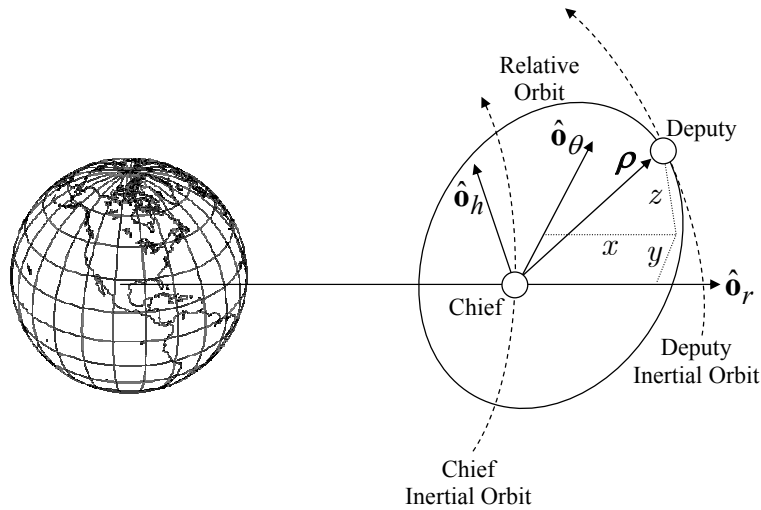


Figure 1. Local Hill Frame Coordinates for Relative Orbit Trajectories

chief spacecraft by the full nonlinear equations of motion as¹²

$$\ddot{x} - x\dot{\nu}^2 \left(1 + 2\frac{r_c}{p}\right) - 2\dot{\nu} \left(\dot{y} - y\frac{\dot{r}_c}{r_c}\right) = 0 \quad (1a)$$

$$\ddot{y} + 2\dot{\nu} \left(\dot{x} - x\frac{\dot{r}_c}{r_c}\right) - y\dot{\nu}^2 \left(1 - \frac{r_c}{p}\right) = 0 \quad (1b)$$

$$\ddot{z} + \frac{r_c}{p}\dot{\nu}^2 z = 0 \quad (1c)$$

where $\dot{\nu}$ is the rate of change of the true anomaly, r_c is the magnitude of the chief spacecraft's position and p is the the semilatus rectum of the chief. Two more differential equations are required for the chief radius and true anomaly:

$$\ddot{r}_c = r_c\dot{\nu}^2 \left(1 - \frac{r_c}{p}\right) \quad (2a)$$

$$\ddot{\nu} = -2\frac{\dot{r}_c}{r_c}\dot{\nu} \quad (2b)$$

Equations (1) and (2) require initial conditions for x , y , z , r_c , ν and their respective derivatives.

For near circular orbits with small relative distances these equations can be simplified to the linearized equations of motion for relative orbital dynamics, which are commonly referred to as the Clohessy-Wiltshire (CW) equations:

$$\ddot{x} - 2n\dot{y} - 3n^2x = 0 \quad (3a)$$

$$\ddot{y} + 2n\dot{x} = 0 \quad (3b)$$

$$\ddot{z} + n^2z = 0 \quad (3c)$$

where n is the mean motion. Note that the last equation is decoupled from the first two. Both the linear and nonlinear equations are used to demonstrate the proof of concept in this paper.

B. Measurements

The goal of this paper is to prove that relative navigation can be accomplished with a photometric sensor onboard the chief spacecraft. The measurements that can be made with such a sensor are the azimuth and elevation angles to the deputy spacecraft and the light intensity that is reflected off of the deputy spacecraft towards the chief spacecraft. By knowing the position of the sensor on the chief spacecraft, the LOS vector

to the deputy can be determined. This can be done very simply by determining where on the photosensor the deputy spacecraft is seen. The sensor can also record the light intensity that is being reflected from the deputy spacecraft back to the chief spacecraft, which will allow for the state estimation of the deputy's position and velocity with respect to the chief.

For the simulations performed in this paper it is assumed that the deputy spacecraft is in view of the Sun reflecting light off its body towards the chief spacecraft as seen in Figure 2. The photometric sensor on the chief spacecraft, which in this illustration is pointed along the $\hat{\mathbf{c}}_1$ axis, will be able to measure the intensity of the light being reflected. Since the location of the sensor onboard the chief spacecraft is known, the angles that point to the deputy can be measured. This method assumes that the surface properties and shape of the deputy spacecraft are known; therefore it will only work for collaborative formation flying spacecraft.

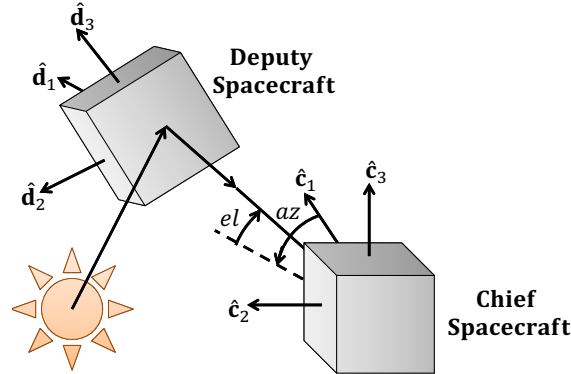


Figure 2. Reflection Pattern from Sun Off Deputy to Chief Spacecraft

As previously mentioned, the sensor measurements being used for this proof of concept are light intensity, m_{app} , and the azimuth and elevation angles, az and el , respectively. The following equations are used to generate the observations:

$$\|\boldsymbol{\rho}\| = \sqrt{x^2 + y^2 + z^2} \quad (4a)$$

$$az = \tan^{-1}\left(\frac{y}{x}\right) \quad (4b)$$

$$el = \sin^{-1}\left(\frac{z}{\|\boldsymbol{\rho}\|}\right) \quad (4c)$$

Here, $\|\boldsymbol{\rho}\|$ is the relative range between the space vehicles. The angles are simple trigometric functions that determine the direction of the LOS to the deputy. In order for the light intensity to be calculated, the photon flux needs to be determined. The photon flux is the number of solar photons reflected off of the deputy spacecraft in the direction of the photometric sensor onboard the chief spacecraft. For this initial proof of concept the photon flux, F , can be modeled with a very simple diffuse spherical model given by¹³

$$F = F_{sun} \frac{R_{diff} A}{\|\boldsymbol{\rho}\|^2} (1 + \mathbf{u}_{obs} \cdot \mathbf{u}_{sun}) \quad (5)$$

where $F_{sun} = 455 \text{ W/m}^2$ is the power per square meter impinging on a given object due to visible light from the Sun striking the surface and A is the area of the spacecraft facing the Sun, which will be assumed as πr^2 where r is the approximate radius of the spacecraft. The term R_{diff} is the diffuse parameter. For a fully diffuse body $R_{diff} = 1$, which is assumed in this paper. Equation (5) assumes that the deputy spacecraft is a simple sphere, which eliminates the spacecraft orientation from affecting the light intensity measurements in this proof of concept. While light will generally reflect off a surface spectrally and diffusely, here only the diffuse term is considered in order to avoid the complexities associated with light glints and imperfections in the surface material. In Eq. (5) \mathbf{u}_{obs} is the LOS vector from the deputy to the observing sensor on the chief and \mathbf{u}_{sun} is the LOS vector from the deputy to the Sun. The photon flux is now used to compute the apparent brightness magnitude, which in practice is measured by a photometric sensor onboard the chief spacecraft:

$$m_{app} = -26.7 - 2.5 \log_{10} \left| \frac{F}{F_{sun}} \right| \quad (6)$$

where -26.7 is the apparent magnitude of the Sun and F_{sun} is the photon flux of the Sun at the Earth, as defined above. In Eq. (6), m_{app} is the apparent magnitude that is being observed reflecting off of the deputy spacecraft. This is the light curve data that will allow the position and velocity to be estimated. The observation vector is then given by $\mathbf{y}(t) = [m_{\text{app}} \text{ az } \text{el}]^T$.

C. Unscented Kalman Filtering

A UKF is selected for this state estimation problem because it is associated with less error than the Extended Kalman Filter (EKF) and does not require the calculation of the Jacobian matrix as required by the EKF. Furthermore, this initial proof of concept incorporates the full nonlinear equations of relative motion for formation flying spacecraft and in this case the UKF is associated with a higher-order of accuracy. Additionally, in future analysis when more complex light intensity models are simulated, such as models with multiple facets or wrinkled surfaces, the Jacobian matrix will become problematic to compute whereas with the UKF this calculation is unnecessary.

The state vector is given by $\mathbf{x}(t) = [x \ y \ z \ \dot{x} \ \dot{y} \ \dot{z} \ r_c \ \dot{r}_c \ \nu \ \dot{\nu}]^T$ for the nonlinear system case shown in Eqs. (1) and (2), and $\mathbf{x}(t) = [x \ y \ z \ \dot{x} \ \dot{y} \ \dot{z}]^T$ for the linear system model case shown by Eq. (3). The UKF process has been well documented and has been accomplished with the following procedure.¹⁴ The relative equations of motion can be written as a general state equation of the form:

$$\mathbf{x}_{k+1} = \mathbf{f}(\mathbf{x}_k, \mathbf{w}_k, \mathbf{u}_k, k) \quad (7a)$$

$$\tilde{\mathbf{y}}_k = \mathbf{h}(\mathbf{x}_k, \mathbf{u}_k, \mathbf{v}_k, k) \quad (7b)$$

where \mathbf{u}_k is a known control input, which is zero for the relative navigation problem. Note that a continuous-time model can always be written using Eq. (7a) through an appropriate numerical integration scheme. As with the Kalman filter it is assumed that \mathbf{w}_k and \mathbf{v}_k are zero-mean Gaussian noise processes with covariances given by Q_k and R_k , respectively. The Kalman filter update equations are first rewritten as

$$\hat{\mathbf{x}}_k^+ = \hat{\mathbf{x}}_k^- + K_k \mathbf{e}_k^- \quad (8a)$$

$$P_k^+ = P_k^- - K_k P_k^{e_y e_y} K_k^T \quad (8b)$$

where the innovations process is given by

$$\mathbf{e}_k^- \equiv \tilde{\mathbf{y}}_k - \hat{\mathbf{y}}_k^- \quad (9)$$

The covariance of \mathbf{e}_k^- is defined by $P_k^{e_y e_y}$. The gain K_k is computed using

$$K_k = P_k^{e_x e_y} (P_k^{e_y e_y})^{-1} \quad (10)$$

where $P_k^{e_x e_y}$ is the cross-correlation matrix.

The UKF uses a different propagation than the form given by the standard EKF. Given an $n \times n$ covariance matrix P , a set of order n points can be generated from the columns (or rows) of the matrices $\pm \sqrt{nP}$. The set of points is zero mean, but if the distribution has mean $\boldsymbol{\mu}$, then simply adding $\boldsymbol{\mu}$ to each of the points yields a symmetric set of $2n$ points having the desired mean and covariance.¹⁵ Due to the symmetric nature of this set, its odd central moments are zero, so its first three moments are the same as the original Gaussian distribution. This is the foundation for the UKF. A complete derivation of this filter is beyond the scope of the present text, so only the final results are presented here. Various methods can be used to handle the process noise and measurement noise in the UKF. One approach involves augmenting the covariance matrix with

$$P_k^a = \begin{bmatrix} P_k^+ & P_k^{xw} & P_k^{xv} \\ (P_k^{xw})^T & Q_k & P_k^{wv} \\ (P_k^{xv})^T & (P_k^{wv})^T & R_k \end{bmatrix} \quad (11)$$

where P_k^{xw} is the correlation between the state error and process noise, P_k^{xv} is the correlation between the state error and measurement noise, and P_k^{wv} is the correlation between the process noise and measurement noise, which are all zero for most systems. Augmenting the covariance requires the computation of $2(q + \ell)$ additional sigma points (where q is the dimension of \mathbf{w}_k and ℓ is the dimension of \mathbf{v}_k , which does not

necessarily have to be the same dimension, m , as the output in this case), but the effects of the process and measurement noise in terms of the impact on the mean and covariance are introduced with the same order of accuracy as the uncertainty in the state.

The general formulation for the propagation equations is given as follows. First, the following set of *sigma points* is computed:

$$\boldsymbol{\sigma}_k \leftarrow 2L \text{ columns from } \pm\gamma\sqrt{P_k^a} \quad (12a)$$

$$\boldsymbol{\chi}_k^{a(0)} = \hat{\mathbf{x}}_k^a \quad (12b)$$

$$\boldsymbol{\chi}_k^{a(i)} = \boldsymbol{\sigma}_k^{(i)} + \hat{\mathbf{x}}_k^a \quad (12c)$$

where $\hat{\mathbf{x}}_k^a$ is an augmented state defined by

$$\mathbf{x}_k^a = \begin{bmatrix} \mathbf{x}_k \\ \mathbf{w}_k \\ \mathbf{v}_k \end{bmatrix}, \quad \hat{\mathbf{x}}_k^a = \begin{bmatrix} \hat{\mathbf{x}}_k \\ \mathbf{0}_{q \times 1} \\ \mathbf{0}_{\ell \times 1} \end{bmatrix} \quad (13)$$

and L is the size of the vector $\hat{\mathbf{x}}_k^a$. The parameter γ is given by

$$\gamma = \sqrt{L + \lambda} \quad (14)$$

where the composite scaling parameter, λ , is given by

$$\lambda = \alpha^2(L + \kappa) - L \quad (15)$$

The constant α determines the spread of the sigma points and is usually set to a small positive value (e.g., $1 \times 10^{-4} \leq \alpha \leq 1$).¹⁶ Also, the significance of the parameter κ will be discussed shortly. Efficient methods to compute the matrix square root can be found by using the Cholesky decomposition. If an orthogonal matrix square root is used, then the sigma points lie along the eigenvectors of the covariance matrix. Note that there are a total of $2L$ values for $\boldsymbol{\sigma}_k$ (the positive and negative square roots). The transformed set of sigma points is evaluated for each of the points by

$$\boldsymbol{\chi}_{k+1}^{x(i)} = \mathbf{f}(\boldsymbol{\chi}_k^{x(i)}, \boldsymbol{\chi}_k^{w(i)}, \mathbf{u}_k, k) \quad (16)$$

where $\boldsymbol{\chi}_k^{x(i)}$ is a vector of the first n elements of $\boldsymbol{\chi}_k^{a(i)}$, and $\boldsymbol{\chi}_k^{w(i)}$ is a vector of the next q elements of $\boldsymbol{\chi}_k^{a(i)}$, with

$$\boldsymbol{\chi}_k^{a(i)} = \begin{bmatrix} \boldsymbol{\chi}_k^{x(i)} \\ \boldsymbol{\chi}_k^{w(i)} \\ \boldsymbol{\chi}_k^{v(i)} \end{bmatrix} \quad (17)$$

where $\boldsymbol{\chi}_k^{v(i)}$ is a vector of the last l elements of $\boldsymbol{\chi}_k^{a(i)}$, which will be used to compute the output covariance. We now define the following weights:

$$W_0^{\text{mean}} = \frac{\lambda}{L + \lambda} \quad (18a)$$

$$W_0^{\text{cov}} = \frac{\lambda}{L + \lambda} + (1 - \alpha^2 + \beta) \quad (18b)$$

$$W_i^{\text{mean}} = W_i^{\text{cov}} = \frac{1}{2(L + \lambda)}, \quad i = 1, 2, \dots, 2L \quad (18c)$$

where β is used to incorporate prior knowledge of the distribution (a good starting guess is $\beta = 2$).

The predicted mean for the state estimate is calculated using a weighted sum of the points $\boldsymbol{\chi}_k^{x(i)}$, which is given by

$$\hat{\mathbf{x}}_k^- = \sum_{i=0}^{2L} W_i^{\text{mean}} \boldsymbol{\chi}_k^{x(i)} \quad (19)$$

The predicted covariance is given by

$$P_k^- = \sum_{i=0}^{2L} W_i^{\text{cov}} [\boldsymbol{\chi}_k^{x(i)} - \hat{\boldsymbol{x}}_k^-] [\boldsymbol{\chi}_k^{x(i)} - \hat{\boldsymbol{x}}_k^-]^T \quad (20)$$

The mean observation is given by

$$\hat{\boldsymbol{y}}_k^- = \sum_{i=0}^{2L} W_i^{\text{mean}} \boldsymbol{\gamma}_k^{(i)} \quad (21)$$

where

$$\boldsymbol{\gamma}_k^{(i)} = \mathbf{h}(\boldsymbol{\chi}_k^{x(i)}, \mathbf{u}_k, \boldsymbol{\chi}_k^{v(i)}, k) \quad (22)$$

The output covariance is given by

$$P_k^{yy} = \sum_{i=0}^{2L} W_i^{\text{cov}} [\boldsymbol{\gamma}_k^{(i)} - \hat{\boldsymbol{y}}_k^-] [\boldsymbol{\gamma}_k^{(i)} - \hat{\boldsymbol{y}}_k^-]^T \quad (23)$$

Then, the innovations covariance is simply given by

$$P_k^{e_y e_y} = P_k^{yy} \quad (24)$$

Finally the cross-correlation matrix is determined using

$$P_k^{e_x e_y} = \sum_{i=0}^{2L} W_i^{\text{cov}} [\boldsymbol{\chi}_k^{x(i)} - \hat{\boldsymbol{x}}_k^-] [\boldsymbol{\gamma}_k^{(i)} - \hat{\boldsymbol{y}}_k^-]^T \quad (25)$$

The filter gain is then computed using Eq. (10), and the state vector can now be updated using Eq. (8). Even though propagations on the order of $2n$ are required for the UKF, the computations may be comparable to the EKF (especially if the continuous-time covariance equation needs to be integrated and a numerical Jacobian matrix is evaluated). Also, if the measurement noise, \mathbf{v}_k , appears linearly in the output (with $\ell = m$), which is the case in this paper, then the augmented state can be reduced because the system state does not need to be augmented with the measurement noise. In this case the covariance of the measurement error is simply added to the innovations covariance, with

$$P_k^{e_y e_y} = P_k^{yy} + R_k \quad (26)$$

This can greatly reduce the computational requirements in the UKF.

The scalar κ in the previous set of equations is a convenient parameter for exploiting knowledge (if available) about the higher moments of the given distribution.¹⁷ In scalar systems (i.e., for $L = 1$), a value of $\kappa = 2$ leads to errors in the mean and variance that are sixth order. For higher-dimensional systems choosing $\kappa = 3 - L$ minimizes the mean squared error up to the fourth order.¹⁵ However, caution should be exercised when κ is negative since a possibility exists that the predicted covariance can become non-positive semi-definite.

III. Simulation Results

A. Linear Model Simulation

In order to prove the new concept for relative navigation, a simulation study is conducted to show that the assumed measurements can be used to adequately track the deputy spacecraft relative to the chief spacecraft. For this simulation the initial positions and velocities of a chief spacecraft and deputy spacecraft are assigned by using identical orbital elements with the exception of eccentricity. The orbits are nearly circular since they have small eccentricities and there are small relative distances between the spacecraft. This means that these orbits do not violate the assumptions that are used for deriving the CW equations, which are a small relative distance and a nearly circular chief orbit. The initial condition used to propagate the CW equations is given by

$$\mathbf{x}_0 = \begin{bmatrix} 42.164 & 0 & 0 & 0 & -6.1301 \times 10^{-3} & -5.6629 \times 10^{-4} \end{bmatrix}^T \quad (27)$$

The chief orbit is assumed to be a geosynchronous one. No process noise is added to the true state.

The measurement covariance matrix is given by $R = \text{diag}[0.1, 0.0085^\circ, 0.0085^\circ]$ and the initial covariance matrix is given by $P_0 = \text{diag}[1 \times 10^1, 4 \times 10^1, 1 \times 10^1, 1 \times 10^{-2}, 4 \times 10^{-2}, 1 \times 10^{-2}]$. These are associated with 1 km errors in the x and z axis and 4 km in the y axis in the position and errors of the order of 10 m/s in the velocity. For this simulation the measurements are generated assuming the deputy spacecraft to be a simple sphere with a 2 meter radius. These initial conditions produce the following results using the filtering procedure described in the previous section.

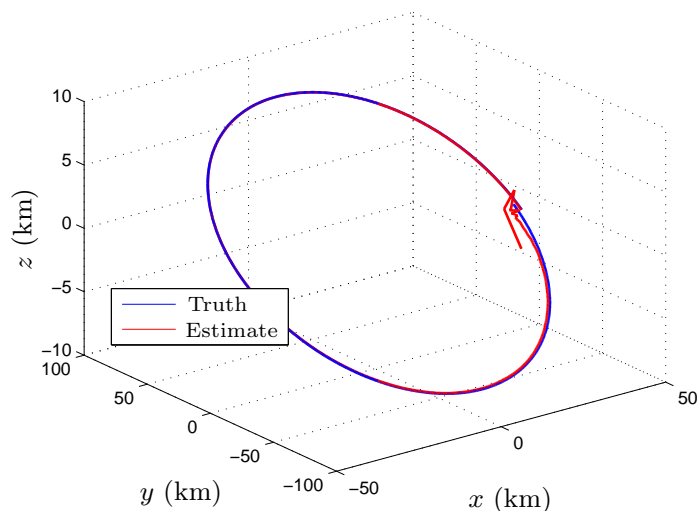


Figure 3. Relative Orbit Trajectories for the CW Case

In Figure 3 it is seen that the relative orbit is nearly a closed circular orbit. This figure also shows that the relative orbit is small with the maximum displacement of the deputy from the chief spacecraft being less than 100 km. The large errors seen in this figure are due to the large initial condition errors injected into the filter initial estimates. In Figure 4(a) it is seen that the errors associated with the position are quickly minimized and settle to approximately 100 m. These values are well within the 3σ bounds shown as the dashed line. The same can be seen for the errors associated with the velocity in Figure 4(b); they are of the order 0.01 m/s. This indicates that the filtering process is successful in tracking the deputy spacecraft for the duration of the orbit.

To gain a better understanding of what is occurring in the simulation the light intensity is plotted in Figure 5. It is seen that the magnitude of the intensity changes with respect to time. This is because as the space vehicles change position in time the relative distance increases then decreases again. As the relative distance decreases between the space vehicles the magnitude of the light intensity decreases; similarly as the magnitude begins to increase so does the relative distance. This is because the brighter an object is the more negative its magnitude light intensity. When Figures 4(a), 4(b) and 5 are compared it can be seen that when the light intensity increases the 3σ bounds begin to grow. This is because the strength of the magnitude measurement is getting weaker and therefore the measurement update in the filtering process is less helpful. This is when the filter relies on the dynamical model for its state estimation.

Figure 6 shows various quantities that produce the light intensity shown in Figure 5. Specifically, Figure 6(a) shows the photon flux data given by Eq. (5). Figure 6(b) shows the dot product between the Sun and observer vectors. Figure 6(c) shows the relative range between the vehicles. Figure 6(d) shows the angle between the LOS and velocity vector, which corresponds the classic case seen in relative navigation where these vectors are nearly perpendicular at all times.^{18,19} Figure 6(b) shows that the motion of the Sun can cause a change in the flux, which has a cycle of one day. This is due to the fact that the chief is in a geosynchronous orbit. The value of this dot product is independent of the relative range shown in Figure 6(c), which depends strictly on the relative motion between the vehicles. Note that the flux is a function of the inverse of the range squared and the dot product only affects the flux in a proportional manner. Thus, the relative range causes the main fluctuations shown in the flux for this particular case. As the range

increases the flux decreases and conversely as the range decreases the flux increases.

The results in Figures 4(a) and 4(b) show promising performance and are a proof for the concept of using photometric data in a cooperative formation flying system to provide relative navigation information. The reason this would be limited to cooperative flight is because the surface properties and shape of the deputy would need to be known for the measurement model. But as mentioned previously these quantities can also be estimated in the overall process if needed. It has been shown that relative navigation can be accomplished using angles-only information for certain cases; however, if the relative orbits are near circular this approach becomes ill-conditioned since many orbits can produce the same observations. By incorporating the light intensity data this problem can be overcome. In order to illustrate this a Monte Carlo simulation is performed using 200 simulation points. Figure 7 shows the root-mean-square (RMS) average position errors for the case of angles-only (No Mag) and the addition of light curve (Mag) observations for relative navigation. The angles-only case leads to the well-known unobservable case. The relative orbit between the chief and deputy is elliptical in nature, which causes the range variation shown in Figure 6(c), but a family of elliptical solutions is possible from angles-only observations. Note that the angles-only case does not diverge because no process noise is present in the filter. The addition of light curve data provides observability to the filtering process and yields accurate relative position estimates.

B. Nonlinear Model Simulation

In this section the full nonlinear equations of motion for formation flying spacecraft are considered, which are described in Eqs. (1) and (2). The initial conditions for this case are given by

$$\mathbf{x}_0 = \left[200 \quad 200 \quad 100 \quad -0.4 \quad 0 \quad 7.3283 \times 10^3 \quad 0 \quad 0 \quad 0 \right]^T \quad (28)$$

The same theoretical 2 meter radius sphere is used to simulate the deputy spacecraft. A plot of the chief radius is shown in Figure 8. For this case the chief is in a low-Earth non-circular orbit. Therefore, the linear CW equations are not valid. First we will examine the relative trajectories. As seen in Figure 9, the estimated orbit initially has poor predictions for the relative position of the deputy spacecraft; however, this is quickly corrected and the filter begins to accurately track the deputy spacecraft.

The errors in the positions and velocity are plotted in Figures 10(a) and 10(b). Here it is illustrated that after some initial uncertainty all three position errors converge to small values. The remaining uncertainty lie within 100 m of the true value, similar to what is shown in Figure 4(a) for the linear model case. It can also be seen in Figure 10(a) that the errors always lie within the 3σ bounds, which ensures that we have an accurate estimator. In Figure 10(b) the error in the velocity estimates is plotted. Here it can be seen that the estimate errors again lie within the 3σ bounds. The estimates follow the bounds as they fluctuate around with approximately 0.01 m/s uncertainty, similar to Figure 4(b) for the linear simulation.

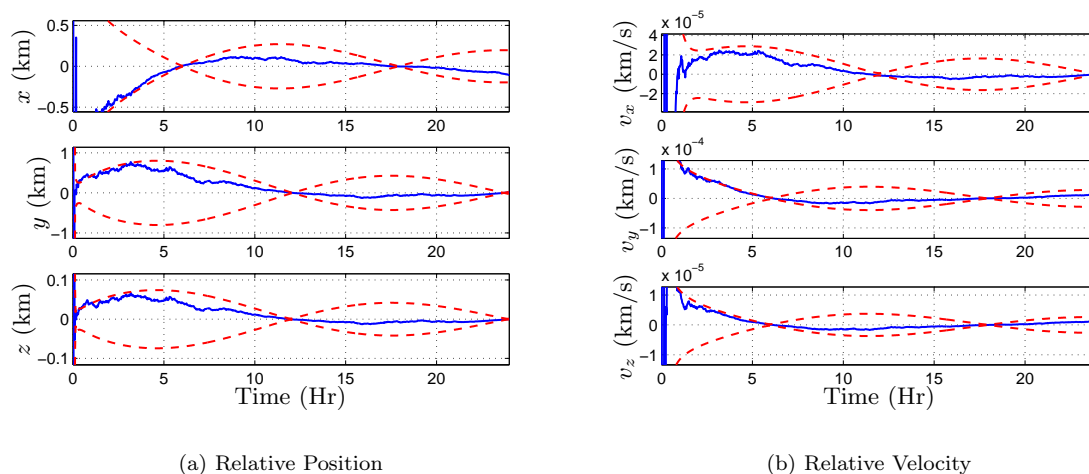


Figure 4. Position and Velocity Estimation Errors for the CW Case

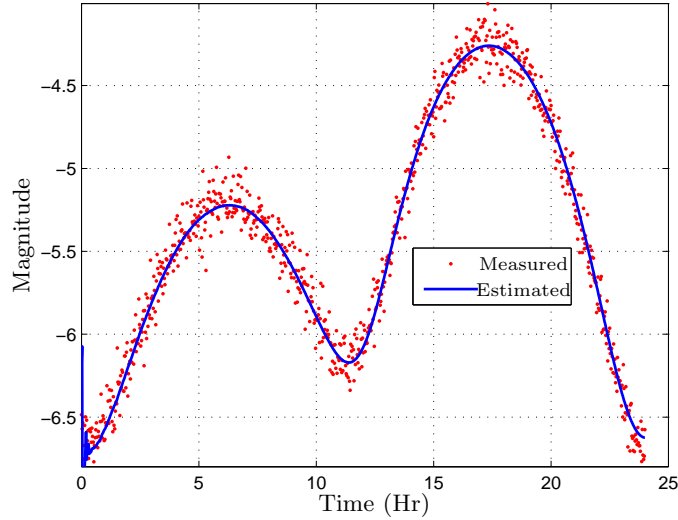


Figure 5. Light Intensity Data

A Monte Carlo simulation is also performed for the nonlinear case. The average RMS position error is calculated and plotted in Figure 12. Here it can be seen that the angles-only approach has oscillations related to the orbital period of nearly 90 minutes. Again, as with the linear case, a converged solution is not possible. But the proposed method of incorporating light curve data decreases the error to below 1 m with less than a half an hour of tracking.

C. Absolute Positions Simulation

References 20 and 21 show that it possible to determine the absolute positions of two spacecraft from relative observations only. Reference 21 uses angles and relative range information to determine the absolute positions. As a final proof of concept, the absolute positions of the chief and deputy spacecraft are calculated using this same navigation technique of angle and light intensity data. The initial conditions are the same as the previous nonlinear model case. It is seen that these are nearly circular orbits that would lie in the low-Earth orbit range and the deputy's orbit varies from the chief spacecraft's orbit with slight variations in the eccentricity, inclination, right ascension to the ascending node, argument of periapsis and mean anomaly.

For this simulation the non-spherical Earth, J_2 , effects are also considered. The acceleration due to the J_2 effect is given by

$$\mathbf{a}_{J_2} = \frac{3}{2} J_2 \left(\frac{\mu}{r^2} \right) \left(\frac{R_{\oplus}}{r} \right)^2 \begin{bmatrix} \left(1 - 5 \left(\frac{z}{r} \right)^2 \right) \frac{x}{r} \\ \left(1 - 5 \left(\frac{z}{r} \right)^2 \right) \frac{y}{r} \\ \left(3 - 5 \left(\frac{z}{r} \right)^2 \right) \frac{z}{r} \end{bmatrix} \quad (29)$$

where $J_2 = 1.082\,626\,683 \times 10^{-3}$ is the coefficient for the second zonal harmonic and $R_{\oplus} = 6,378.137$ km is the mean equatorial radius of the Earth. Note that here x , y and z denote the absolute position coordinates for either the chief or deputy spacecraft and r is the magnitude of these components. When the orbits are plotted in Figure 13, it appears that the estimated trajectory follows the true trajectory. However, since this plot shows the orbital positions throughout the simulation time it is difficult to see how the trajectories differ due to the large scale of the orbit. Therefore, to establish an understanding of how accurate this method is, the error plots are analyzed.

As seen in the error plots in Figure 14 the UKF performs well in tracking the true position and velocity of the spacecraft. In Figure 14(a) it can be seen that there is some fluctuations in the x and z axes. In the y axis, the error is smaller in magnitude and settles faster than other the x and z axes. For this simulation

it is also seen that the 3σ bounds also take longer to tighten around zero. This can also be seen with the 3σ bounds for the errors in velocities in Figure 14(b). Similar results can be seen in Figures 14(c) and 14(d) for the chief spacecraft. Figure 15 shows the absolute average RMS position errors of the deputy for both the angles-only and addition of light curve observation cases. Clearly, the addition of light curve information provides better estimation performance than without it.

IV. Conclusion

This initial proof of concept scenario considers both the simple linearized dynamical model and the full nonlinear equations for the relative motion of the spacecraft, where the simulated measurement data are the light intensity and angles pointing to the deputy spacecraft, and the estimated states and the relative position and velocity. Previous work has shown that it is not possible to track relative motion using angles-only data for certain cases, but the additional information of light intensity was able to improve the accuracy and provide observability to the unobservable cases associated with angles-only tracking. This provides motivation for subsequent studies to investigate the limitations of this new approach. In this further testing more complex measurement models can be used to simulate spacecraft of different shapes and reflective properties. Additionally, the incorporation of attitude estimation will also be explored.

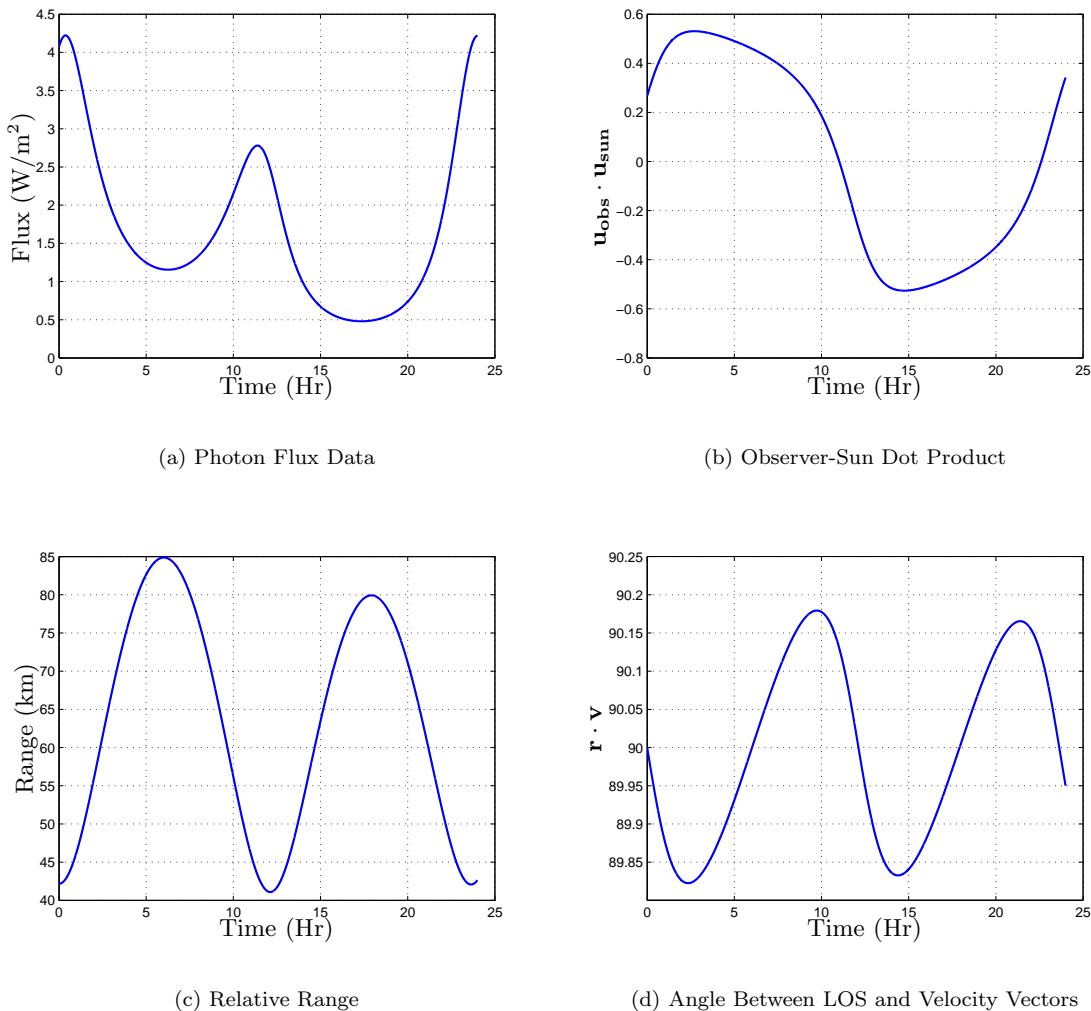


Figure 6. Various Quantities from the Light Intensity Data

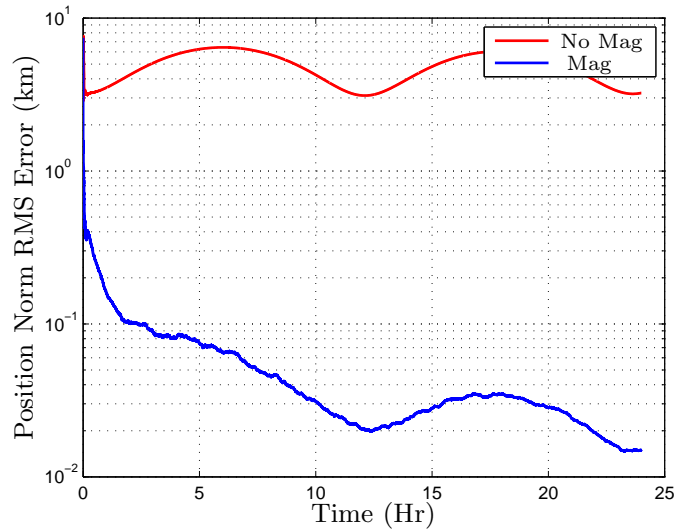


Figure 7. Root Mean Square Error for the CW Case

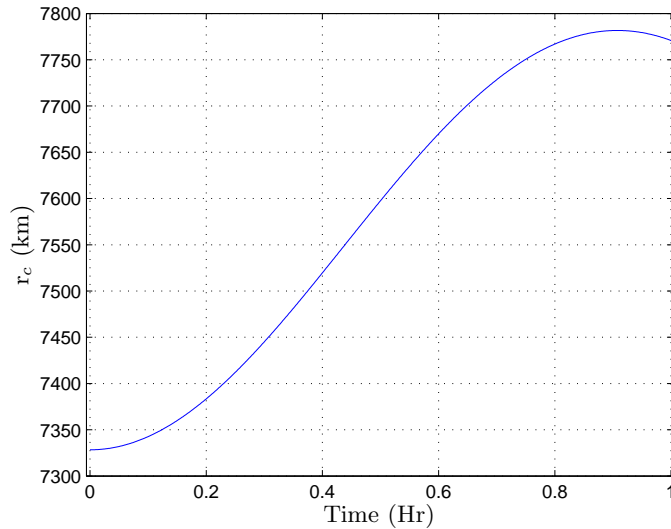


Figure 8. Chief Orbit

This new navigation system will allow for the use of cheaper sensor systems since the only required measurement device is a photometric sensor. These photometric sensors can be of lower quality compared to optical camera systems since only the light intensity needs to be calculated. In other optical systems resolved images need to be used in order to determine the size and orientation of the spacecraft in the image to determine relative distance. This proposed method allows for unresolved images to predict this same motion by utilizing the light intensity. Additionally, it provides a way for the position to be calculated passively, without sending information between the space vehicles.

References

¹Young, G.S. and Chellappa, R., "3-D Motion Estimation Using a Sequence of Noisy Stereo Images: Models, Estimation, and Uniqueness Results," *IEEE Transactions on Pattern Analysis and Machine Intelligence*, Vol. 12, No. 8, Aug. 1990, pp. 735-759.

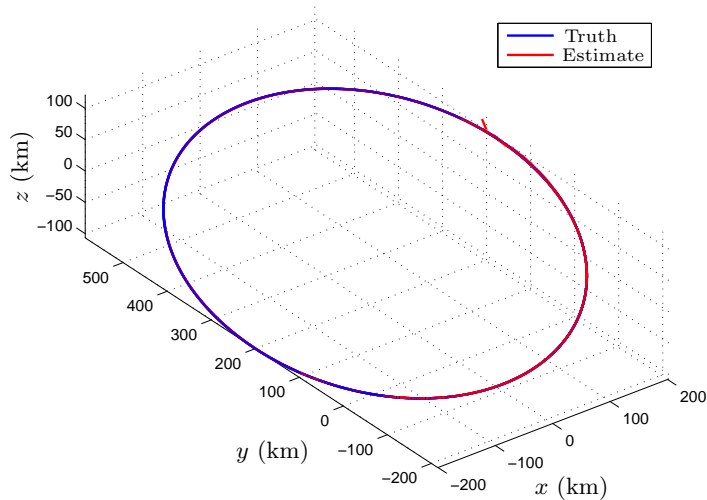


Figure 9. Relative Orbit Trajectories for the Nonlinear Case

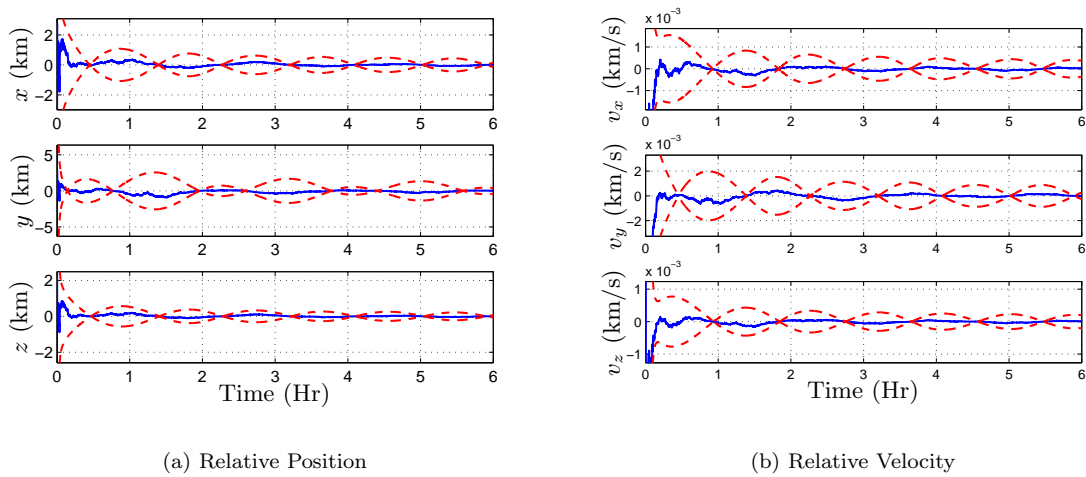


Figure 10. Position and Velocity Estimation Errors for the Nonlinear Case

²Woffinden, D.C. and Geller, D.K., “Relative Angles-Only Navigation and Pose Estimation for Autonomous Orbital Rendezvous,” *Journal of Guidance, Control and Dynamics*, Vol. 30, No. 5, 2007, pp. 1455–1469.

³Broida, T.J. and Chellappa, R., “Estimating the Kinematics and Structure of a Rigid Object from a Sequence of Monocular Images,” *IEEE Transactions on Pattern Analysis and Machine Intelligence*, Vol. 13, No. 6, June 1991, pp. 497–513.

⁴Junkins, J.L., Hughes, D.C., Wazni, K.P., and Pariyapong, V., “Vision-Based Navigation for Rendezvous, Docking and Proximity Operations,” *22nd Annual AAS Guidance and Control Conference*, Breckenridge, CO, Feb. 1999, AAS-99-021.

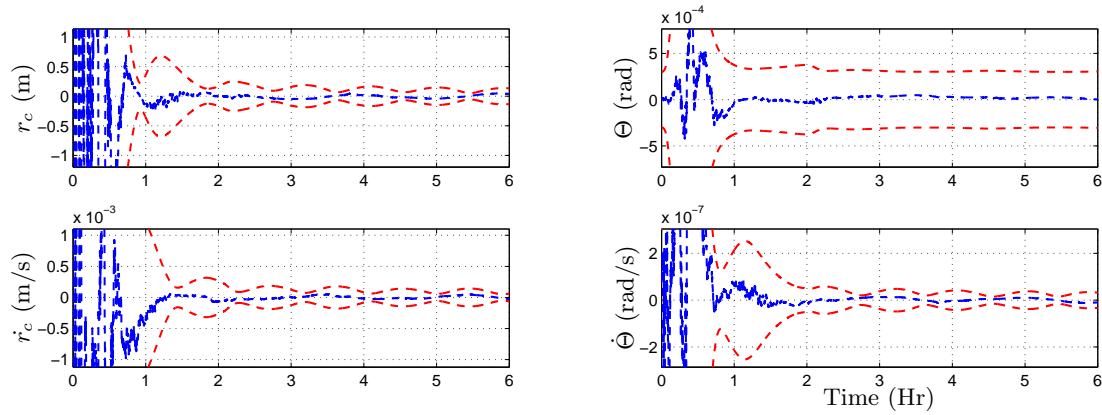
⁵Alonso, R., Crassidis, J.L., and Junkins, J.L., “Vision-Based Relative Navigation for Formation Flying of Spacecraft,” *AIAA Guidance, Navigation, and Control Conference*, Denver, CO, Aug. 2000, AIAA-00-4439.

⁶Kim, S.G., Crassidis, J.L., Cheng, Y., Fosbury, A.M., and Junkins, J.L., “Kalman Filtering for Relative Spacecraft Attitude and Position Estimation,” *Journal of Guidance, Control, and Dynamics*, Vol. 30, No. 1, Jan.-Feb. 2007, pp. 133–143.

⁷Kaasalainen, M. and Torppa, J., “Optimization Methods for Asteroid Lightcurve Inversion I: Shape Determination,” *Icarus*, Vol. 153, No. 4, Jan. 2001, pp. 24–36.

⁸Kaasalainen, M. and Torppa, J., “Optimization Methods for Asteroid Lightcurve Inversion II: The Complete Inverse Problem,” *Icarus*, Vol. 153, No. 4, Jan. 2001, pp. 37–51.

⁹Calef, B., Africano, J., Birge, B., Hall, D., and Kervin, P., “Photometric Signature Inversion,” *Proceedings of the International Society for Optical Engineering*, Vol. 6307, San Diego, CA, Aug. 2006, Paper 11.



(a) Chief Radius

(b) True Anomaly

Figure 11. Chief Radius and True Anomaly Errors for the Nonlinear Case

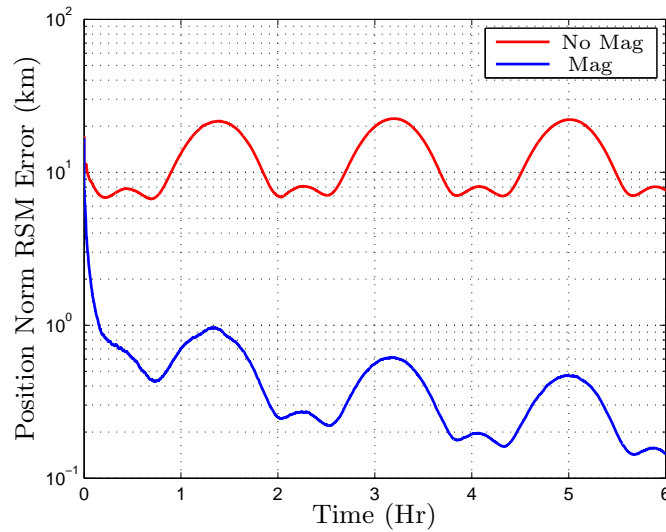


Figure 12. Root Mean Square Errors for the Nonlinear Case

¹⁰Wetterer, C.J. and Jah, M., “Attitude Estimation from Light Curves,” *Journal of Guidance, Control and Dynamics*, Vol. 32, No. 5, Sept.-Oct. 2009, pp. 1648–1651.

¹¹Wetterer, C.J., Chow, C.C., Crassidis, J.L., and Linares, R., “Simultaneous Position Velocity, Attitude, Angular Rates, and Surface Parameter Estimation Using Astrometric and Photometric Observations,” *16th International Conference on Information Fusion*, Istanbul, Turkey, July 2013.

¹²Schaub, H. and Junkins, J.L., *Analytical Mechanics of Aerospace Systems*, American Institute of Aeronautics and Astronautics, Inc., New York, NY, 2003.

¹³Krutz, U., Jahn, H., Kührt, E., Mottola, S., and Spietz, P., “Radiometric Considerations for the Detection of Space Debris with an Optical Sensor in LEO as a Secondary Goal of the Asteroid Finder Mission,” *Acta Astronautica*, Vol. 69, No. 5-6, Sept. 2011, pp. 297–306.

¹⁴Crassidis, J.L. and Junkins, J.L., *Optimal Estimation of Dynamic Systems*, Chapman & Hall, Boca Raton, FL, 2nd ed., 2011.

¹⁵Julier, S.J., Uhlmann, J.K., and Durrant-Whyte, H.F., “A New Approach for Filtering Nonlinear Systems,” *Proceedings of the American Control Conference*, Seattle, WA, June 1995, pp. 1628–1632.

¹⁶Wan, E. and van der Merwe, R., “The Unscented Kalman Filter,” *Kalman Filtering and Neural Networks*, edited by S. Haykin, chap. 7, Wiley, 2001.

¹⁷Bar-Shalom, Y. and Fortmann, T.E., *Tracking and Data Association*, Academic Press, Boston, MA, 1988.

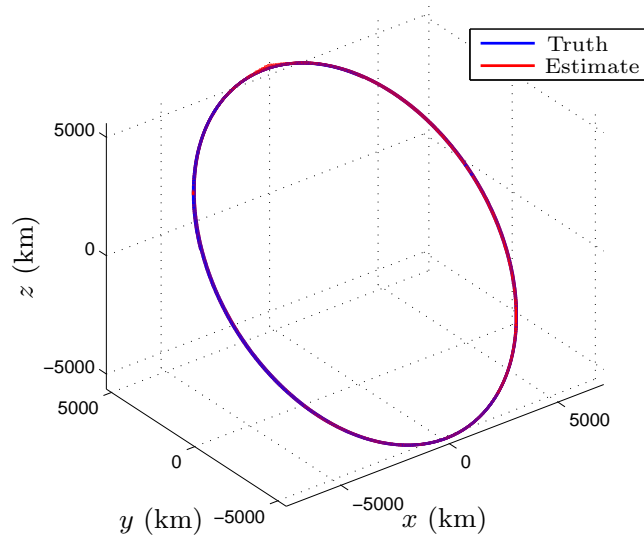


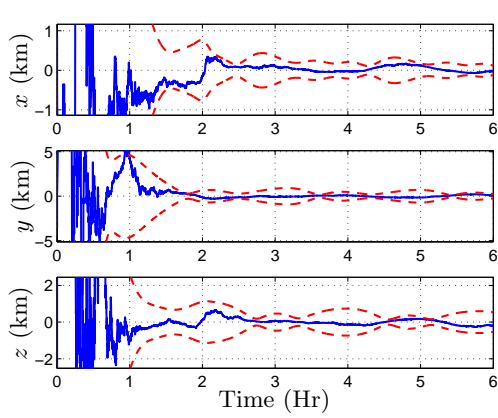
Figure 13. Spacecraft Trajectories for the Absolute Case

¹⁸Doolittle, C.M., Chavez, F.R., and Lovell, T.L., "Relative Orbit Element Estimation for Satellite Navigation," *AIAA Guidance, Navigation and Control Conference*, San Francisco, CA, Aug. 2005, AIAA-2005-6462.

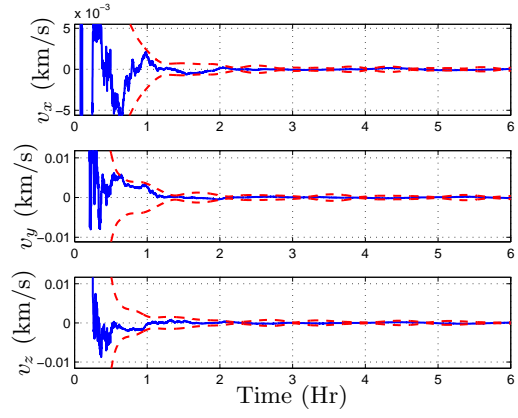
¹⁹Woffinden, D.C. and Geller, D.K., "Observability Criteria for Angles-Only Navigation," *IEEE Transactions on Aerospace and Electronic Systems*, Vol. 45, No. 3, July 2009, pp. 1194–1208.

²⁰Markley, F.L., "Autonomous Satellite Navigation Using Landmark and Intersatellite Data," *AAS/AIAA Astrodynamics Specialist Conference*, Lake Tahoe, NV, Aug. 1981, AAS Paper 81-205.

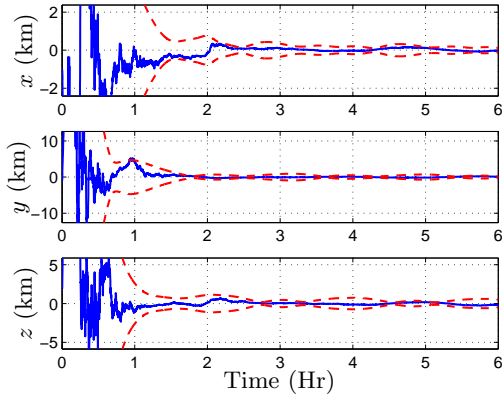
²¹Psiaki, M.L., "Autonomous Orbit Determination for Two Spacecraft from Relative Position Measurements," *Journal of Guidance, Control, and Dynamics*, Vol. 22, No. 2, March-April 1999, pp. 305–312.



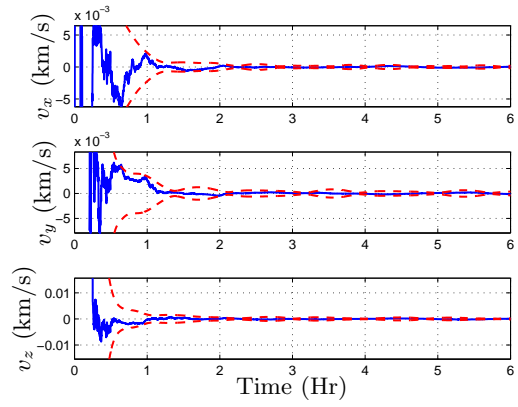
(a) Deputy Position



(b) Deputy Velocity



(c) Chief Position



(d) Chief Velocity

Figure 14. Position and Velocity Estimation Errors for the Absolute Case

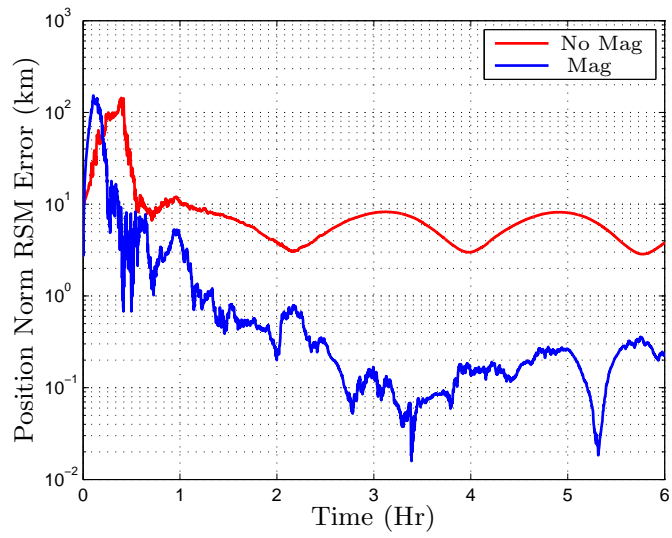


Figure 15. Root Mean Square Error for the Absolute Case